A&A 507, 1475–1484 (2009)
DOI: 10.1051/0004-6361/200912623

Astronomy & Astrophysics

Dissecting an intermediate-mass protostar

Chemical differentiation in IC 1396 N

A. Fuente[1], A. Castro-Carrizo[2], T. Alonso-Albi[1], M. T. Beltrán[3], R. Neri[2], C. Ceccarelli[4], B. Lefloch[4], C. Codella[3], and P. Caselli[5]

[1] Observatorio Astronómico Nacional (OAN), Apdo. 112, 28803 Alcalá de Henares, Madrid, Spain
e-mail: a.fuente@oan.es
[2] Institut de Radioastronomie Millimétrique, 300 rue de la Piscine, 38406 St Martin d'Hères, France
[3] INAF – Osservatorio Astrofisico di Arcetri, Largo E. Fermi 5, 50125 Firenze, Italy
[4] Laboratoire d'Astrophysique, Observatoire de Grenoble, BP 53, 38041 Grenoble Cedex 9, France
[5] School of Physics & Astronomy, University of Leeds, Leeds LS2 9JT, UK

Received 3 June 2009 / Accepted 10 September 2009

ABSTRACT

Aims. We aim to unveil the physical conditions and structure of the intermediate mass (IM) protostar IRAS 21391+5802 (IC 1396 N) on scales of ∼1000 AU.
Methods. We carried out high angular resolution (1.″4) observations in both the continuum at 3.1 mm and the N_2H^+ 1 → 0, CH_3CN $5_k \rightarrow 4_k$ and ^{13}CS 2 → 1 lines using the Plateau de Bure Interferometer (PdBI). In addition, we merged the PdBI images with previous BIMA (continuum data at 1.2 mm and 3.1 mm) and single-dish (N_2H^+ 1 → 0) data to obtain a comprehensive description of the region.
Results. The combination of our data with BIMA and 30 m data show that the associated bipolar outflow has completely eroded the initial molecular globule. The 1.2 mm and 3.1 mm continuum emissions are extended along the outflow axis tracing the warm walls of the biconical cavity. Most of the molecular gas is, however, located in an elongated feature in the direction perpendicular to the outflow. A strong chemical differentiation is detected across the molecular toroid, the N_2H^+ 1 → 0 emission being absent in the inner region.
Conclusions. Our PdBI data show two different regions in IC 1396 N: (i) the young stellar objects (YSO) BIMA 3 and the protocluster BIMA 2, both were detected in dust continuum emission and one of the individual cores in BIMA 2, IRAM 2A, in the CH_3CN $5_k \rightarrow 4_k$ line; and (ii) the clumps and filaments that were only detected in the N_2H^+ 1 → 0 line. The clumps belonging to this second group are located in the molecular toroid perpendicular to the outflow, and mainly along the walls of the biconical cavity. This chemical differentiation can be understood in terms of the different gas kinetic temperature. The CH_3CN abundance towards IRAM 2A is similar to that found in hot corinos and lower than that expected towards IM and high mass hot cores. This indicates that IRAM 2A is a low mass or a Herbig Ae star instead of the precursor of a massive Be star. Alternatively, the low CH_3CN abundance could be the consequence of IRAM 2A being a class 0/I transition object that has already formed a small photodissociation region (PDR).

Key words. stars: formation – stars: individual: IRAS 21391+5802 – stars: individual: IC 1396 N

1. Introduction

Intermediate-mass (IM) young stellar objects (protostars and Herbig Ae/Be stars with $M_\star \sim 2{-}10\ M_\odot$) are crucial to star formation studies because they provide a link between the evolutionary scenarios of low- and high-mass stars. These objects share many similarities with high-mass stars, in particular their predisposition to form in clusters. However, their study has certain advantages over that of massive star forming regions, as many of them are located close to the Sun (≤1 kpc) and in regions of reduced complexity.

IRAS 21391+5802 (IC 1396 N) is one of the most well studied IM protostars (L = 440 $L_\odot$, d = 750 pc). Classified as a class 0/I borderline source, this young protostar is associated with a very energetic bipolar outflow. In addition, near-infrared images by Nisini et al. (2001) and Beltrán et al. (2009) identified a collimated 2.12 μm H_2 jet. The outflows and envelope of this protostar were firstly mapped by Codella et al. (2001) and Beltrán et al. (2002, 2004b) using BIMA and OVRO. These observations detected 3 millimeter continuum sources in the region, the most intense, BIMA 2, being at the center of the envelope and appearing to be the driving source of the most energetic outflow.

Neri et al. (2007) reported high angular resolution continuum images at 3 mm and 1.3 mm carried out with the IRAM Plateau de Bure Interferometer (PdBI) in its most extended configuration. The high sensitivity and spatial resolution of the two continuum images clearly detected three bright continuum emission cores at the position of the source previously named BIMA 2. While the two weaker cores were not resolved by the interferometer, the primary core IRAM 2A was resolved at 1.3 mm emission in an elliptical region of ∼300 AU × 150 AU. The mass and dust emissivity spectral index of this core are similar to those measured in circumstellar disks around Herbig Ae/Be

stars (Neri et al. 2007; Fuente et al. 2003, 2006; Alonso-Albi et al. 2008, 2009). Other possible interpretations (hot corinos, cold compact pre-stellar clumps) cannot, however, be discarded.

In this paper, we present high angular resolution images of the N_2H^+ 1 → 0, CH_3CN $5_k \rightarrow 4_k$ and ^{13}CS $J = 2 \rightarrow 1$ lines observed with the PdBI in its extended AB configuration. In addition, we combine our previous continuum PdBI images (Neri et al. 2007) with the BIMA observations published by Beltrán et al. (2002). The new 1.2 mm and 3.1 mm continuum images together with the molecular data provide a valuable insight into the chemical and physical structure of this IM protocluster, in particular of the IM hot core.

2. Observations

2.1. PdBI observations

Observations were performed with the PdBI in AB configuration between January and March 2008. We observed a 1.4 GHz bandwidth with receivers tuned at 91.78 GHz. The spectral configuration allowed us to achieve a resolution of 0.25 km s^{-1} for the transitions CH_3CN $5_k \rightarrow 4_k$, N_2H^+ 1 → 0 and ^{13}CS 2 → 1. Since the lines are wide, all the maps were created with a spectral resolution of 0.2 MHz (∼0.64 km s^{-1}). The continuum was obtained by averaging the observed band with no line contribution. Because of some poor quality data, the UV-coverage differs slightly for the different lines. Synthesized beams are 1.56″ × 1.23″ PA 68° for CH_3CN, 1.38″ × 1.16″ PA 95° for N_2H^+ and 1.42″ × 1.21″ PA 98° for ^{13}CS. The rms of the images is ∼2.5 mJy/beam (0.2 K).

To calibrate the changes in time of the complex gains (i.e., phases and amplitudes), we observed alternatively with the source, every 22 min, the object 2037+511. The calibration was found to be straightforward for all the tracks. A flux of 1.2 Jy was deduced for 2037+511 at the observed frequency. The RF calibration was performed by observing for a few minutes the brightest sources in the sky. MWC 349 was observed and used as a flux reference by adopting a flux of 1.1 Jy as suggested by PdBI models and to be consistent with the expected antenna efficiency values. The flux calibration was found to be reliable to better than 10%.

2.2. PdBI+BIMA continuum images

The PdBI 3 mm continuum data were merged with previous PdBI data by Neri et al. (2007), and with older interferometric BIMA observations by Beltrán et al. (2002). The contrast in the weights of the different observations makes the merging difficult, forcing us to lower the weights of the PdBI data.

At 1 mm, we merged the PdBI data by Neri et al. (2007) and the BIMA observations by Beltrán et al. (2002). The merging was corrected by the different beam sizes, and no factor was added to correct for the weight contrast. The merged image is only reliable for the innermost 25 arcsec, which corresponds to ∼*HPBW* of the PdBI primary beam. Because of the PdBI primary beam correction, the imaging becomes very noisy close to the border of the PdBI primary beam. Despite there being nearly a factor of 2.5 difference between the primary beam sizes of BIMA and PdBI, we are confident in the elongated structure detected, within the PdBI beam, along the outflow direction.

Finally, we note that the data fluxes were not corrected for the different frequencies of the data sets; the BIMA data frequencies are 97.98 and 244.94 GHz, those of the previous PdBI observations are 92.09 and 242.00 GHz, and the recent 3 mm continuum data are centered on 91.78 GHz. Assuming the largest spectral index measured in the region, alpha = +2.8 (Neri et al. 2007), we could introduce a maximum error in the derived continuum fluxes of ∼30% at 3 mm and ∼10% at 1 mm, which applies mainly to the cocoon.

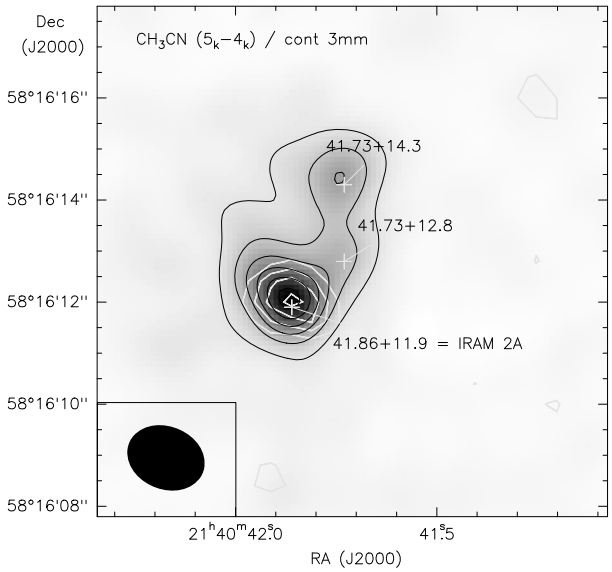

Fig. 1. Integrated intensity maps of the CH_3CN $5_k \rightarrow 4_k$ line (white contours) superposed on the 3 mm continuum image (grey scale map). Contours for the CH_3CN image are from 34 mJy/beam × km s^{-1} (5 × σ) to 75 mJy/beam × km s^{-1} in steps of 9 mJy/beam × km s^{-1}. Contours for the 3 mm continuum image are from 1 mJy/beam to 6 mJy/beam in steps of 1 mJy/beam.

2.3. N_2H^+ 1 → 0 image

The PdBI N_2H^+ data were merged with short-spacing observations obtained with the 30 m-telescope (at Pico Veleta, Spain). A 120″-size field was mapped with the single dish, by observing every ∼12″. As described in Sect. 3.3, the flux is mostly filtered out in the interferometric data. Because that, the single-dish data are so crucial for recovering the flux and reconstructing the line emission distribution.

3. Small scales (≤1000 AU)

3.1. CH_3CN: the hot core IRAM 2A

The CH_3CN $5_k \rightarrow 4_k$ line emission has only been detected towards IRAM 2A, the most massive core in the protocluster. The integrated intensity map of the CH_3CN $5_k \rightarrow 4_k$ transition shows that the emission originates in a point source centered on the position of the massive hot core IRAM 2A (see Fig. 1).

Comparing the integrated emission peak of the PdBI map with that of the 30 m spectrum (see Fig. 2), we estimate that ∼1−2% of the emission originates in a compact region around IRAM 2A while the rest is produced in an extended component. This is approximately the same number we obtain by dividing the 1.3 mm flux towards IRAM 2A, 35 mJy (Neri et al. 2007), and the single-dish 1.3 mm flux, 1.4 Jy. This shows that CH_3CN is a good tracer of IM hot cores.

The interferometric profile of the CH_3CN $5_k \rightarrow 4_k$ emission is very different from that observed with the 30 m telescope (see Fig. 2). In fact, there is a shift of ∼2.5 km s^{-1} between the centroid of the PdBI emission and that of the 30 m.

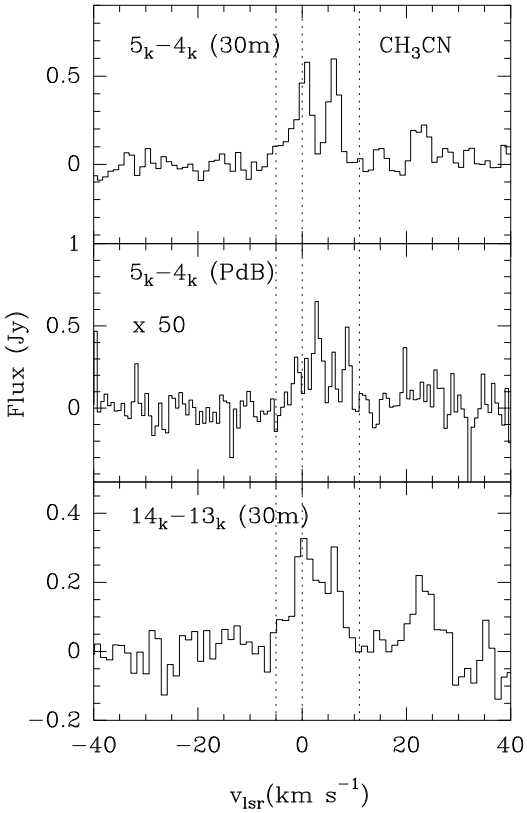

Fig. 2. Spectra of the CH_3CN $5_k \rightarrow 4_k$ and CH_3CN $14_k \rightarrow 13_k$ lines observed with the 30 m and PdBI towards IRAM 2A. Dashed lines indicate the ambient velocity, $v_{lsr} = 0$ km s^{-1}, and the velocities $v_{lsr} = -5$ and 11 km s^{-1} for an easier comparison between the 30 m and PdBI spectra.

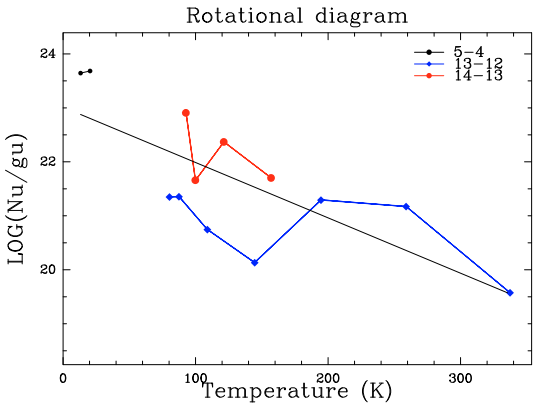

Fig. 3. Rotational diagram of CH_3CN towards IRAM 2A. The rotational diagram has been built using the interferometric CH_3CN $13_k \rightarrow 12_k$ data published by Neri et al. (2007) (blue), those presented in this paper (black), and the CH_3CN $14_k \rightarrow 13_k$ line observed with the 30 m telescope (red).

However, it is much more similar to that observed in the high excitation CH_3CN $14_k \rightarrow 13_k$ line, which suggests that the difference between the single-dish and interferometric profiles of the CH_3CN $5_k \rightarrow 4_k$ line is mainly due to the very different angular resolution of the observations (the beam of the 30 m telescope at the frequency of the CH_3CN $5_k \rightarrow 4_k$ line is ∼27″, the 30 m beam at the frequency of the CH_3CN $14_k \rightarrow 13_k$ is ∼9″, and in our PdBI observations the beam is 1.56″ × 1.23″). This also suggests that the velocity of the hot core is different from that of the bulk of the molecular cloud. Most of the CH_3CN $5_k \rightarrow 4_k$ single-dish emission originates in the extended envelope whose kinematics have been severely affected by the bipolar outflow (see Codella et al. 2001; Beltrán et al. 2002, 2004b). However, the different velocity profiles of the PdBI and 30 m lines could also be caused by the filtering of the extended emission by the PdBI observations. The amount of missed flux is different for each spectral channel depending on the spatial distribution of the emission at that velocity. Interferometric observations at lower angular resolution are required to discern the filtering effects and any difference in velocity between the hot core and the surrounding cloud.

We determined the CH_3CN column density towards IRAM 2A using the rotational diagram technique and the interferometric CH_3CN $13_k \rightarrow 12_k$ data published by Neri et al. (2007), those presented in this paper and the CH_3CN $14_k \rightarrow 13_k$ line observed with the 30 m telescope (see Fig. 3). We assume that all the emission of the CH_3CN $14_k \rightarrow 13_k$ line originates in the hot core IRAM 2A. If an extended emission component also contributes to the flux of the CH_3CN $14_k \rightarrow 13_k$ line, the derived temperature is an upper limit to the true value. We derive a rotational temperature of 97 ± 25 K and a CH_3CN column density of 6.5 ± 5.0 × 10^{13} cm^{-2} averaged in a beam of 1.6″ × 1.2″. Assuming that the dust temperature is 100 K, and the size of IRAM 2A estimated by Neri et al. (2007), 0.4″ × 0.2″, we obtain a CH_3CN abundance of 5 ± 3 × 10^{-10} in this core.

3.2. ^{13}CS

We have not detected the ^{13}CS 2 → 1 line in this region. Beltrán et al. (2004b) mapped the region in the CS $J = 2 \rightarrow 1$ line using BIMA with an angular resolution of ∼7.0″ × 6.3″. The most intense peak is detected towards BIMA 2 with a maximum intensity of 9.6 Jy beam^{-1} km s^{-1}, integrated in a velocity interval of −3 to 3 km s^{-1}. Assuming that the line ratio of the ^{12}CS 2 → 1/^{13}CS 2 → 1 is ∼60 (a reasonable value for N(CS) = 2 × 10^{14} cm^{-2} derived by Codella et al. 2001), our upper limit to the ^{13}CS emission implies that less than 60% of the CS emission detected by the BIMA interferometer originates in the IM hot core. In the case of lower ^{12}CS 2 → 1/^{13}CS 2 → 1 line ratio, i.e., a higher opacity of the CS 2 → 1 line, the fraction of the ^{13}CS emission that originates in the hot core would be smaller. Thus, the ^{13}CS 2 → 1 line does not seem to be a good tracer of IM hot cores. This is consistent with the kinematical study by Beltrán et al. (2004b). They concluded that the CS emission does not trace the dense hot core, but instead the interaction of the molecular outflow with the core(s).

3.3. N_2H^+

In Fig. 4, we show the integrated intensity maps of the N_2H^+ $J = 1 \rightarrow 0$ $F = 1 \rightarrow 1$, $F = 2 \rightarrow 1$, and $F = 0 \rightarrow 1$ lines. Emission of the N_2H^+ line has been detected in several clumps across the area sampled by the interferometer (labeled N in Fig. 4), but none of them is spatially coincident with the compact cores detected in the continuum images (see Fig. 5). Moreover, the interferometric spectrum towards the most intense core, IRAM 2A, shows no evidence of emission. We convolved the entire image with a beam of 27″ before comparing the result with the single-dish spectrum obtained with the 30 m by Alonso-Albi et al. (2009, in preparation). We found that only 1% of the flux was recovered by the interferometer. The velocity profile of the PdBI and 30 m spectra also differ considerably indicating that most of the

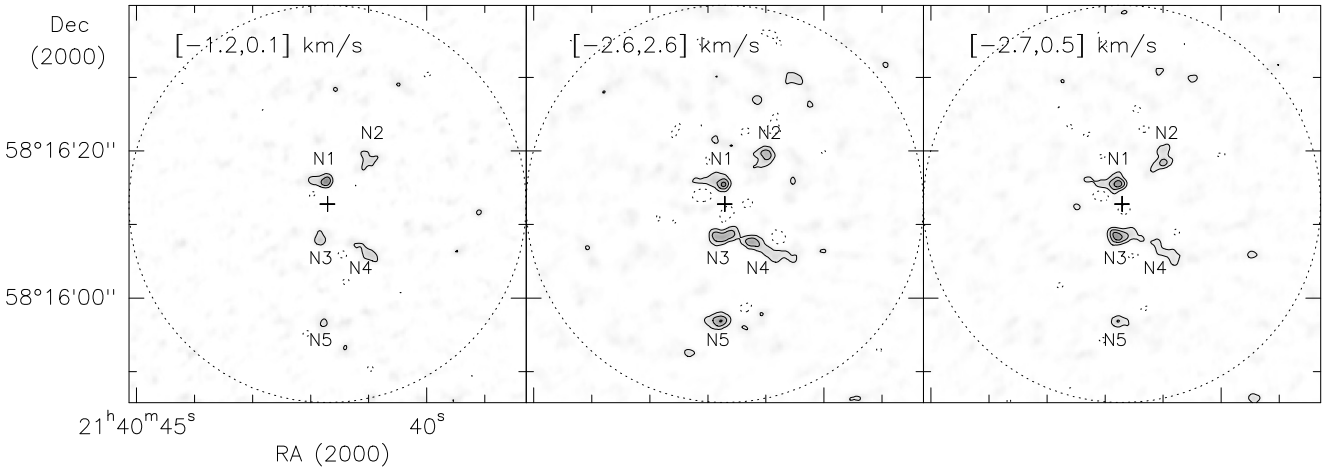

Fig. 4. Integrated intensity images of the N_2H^+ $J = 1 \rightarrow 0$ $F = 1 \rightarrow 1$ (*left*), $F = 2 \rightarrow 1$ (*middle*) and $F = 0 \rightarrow 1$ (*right*) lines. First contour and contour spacing is $3 \times \sigma$, where σ is 4.2 mJy/beam (*left*), 9.1 mJy/beam (*middle*), and 6.0 mJy/beam (*right*). The primary beam (≈54″) is indicated by a dotted circle.

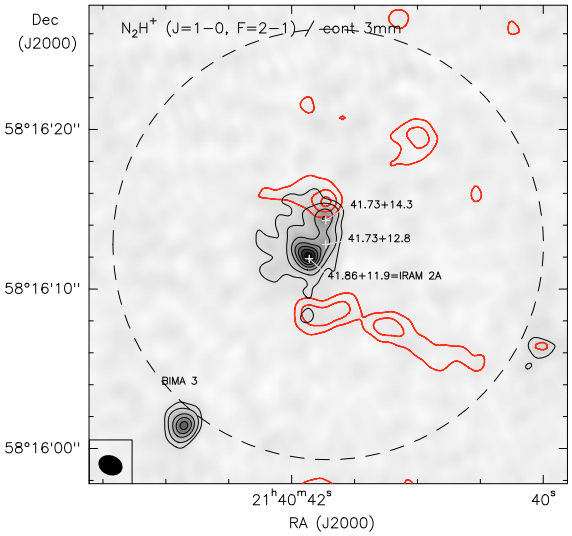

Fig. 5. Integrated intensity map of the N_2H^+ $1 \rightarrow 0$ $F = 2 \rightarrow 1$ line (red contours) superposed on the 3 mm continuum image (grey scale map). Contours of the N_2H^+ $1 \rightarrow 0$ $F = 2 \rightarrow 1$ line are the same as in Fig. 4. Contours of the 3.1 mm continuum emission are 0.5 mJy/beam, and from 1 mJy/beam to 6 mJy/beam in steps of 1 mJy/beam. The primary beam is indicated by a dashed line.

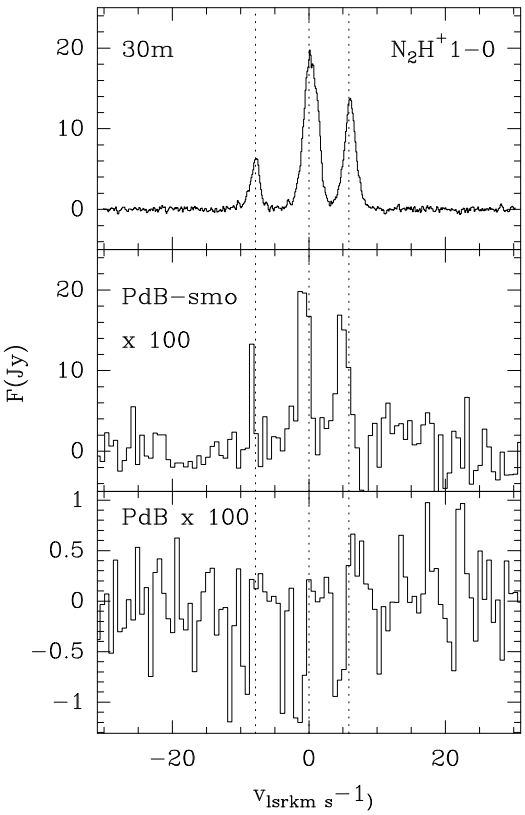

Fig. 6. The spectrum of the N_2H^+ $1 \rightarrow 0$ line obtained from our interferometric images towards IRAM 2A is shown in the *bottom panel*. In the *middle panel*, we show the spectrum obtained after convolving the interferometric N_2H^+ $1 \rightarrow 0$ image with a beam of 27″. In the *upper panel*, we show the spectrum of the same line obtained within the 30 m telescope. Dashed lines indicate the position of the $F = 1 \rightarrow 1$, $F = 2 \rightarrow 1$, and $F = 0 \rightarrow 1$ hyperfine components.

emission at ambient and redshifted velocities was resolved and filtered out by the PdBI observations (see Fig. 6).

In Fig. 7, we show our N_2H^+ $1 \rightarrow 0$ $F = 2 \rightarrow 1$ image superposed to the bipolar molecular outflow traced by the interferometric observations of the CO $1 \rightarrow 0$ and CS $5 \rightarrow 4$ lines. All the N_2H^+ clumps except N5 seem to follow the morphology of the bipolar outflow, delineating the walls of the cavity. That filtering is less important at velocities offset from that of the ambient cloud, improves the detection of the interaction layer between the outflow and the surrounding cloud. The agreement between N_2H^+ and the bipolar outflow lobes is closer when we compare with the CS $5 \rightarrow 4$ line. This is expected because N_2H^+ and CS are high dipole moment molecules that trace the dense gas. If we take into account the lower angular resolution of the CS data, CS and N_2H^+ could have a similar spatial distribution in the blue lobe.

4. Large scale

4.1. PdBI+BIMA continuum images

The continuum images at 1.2 mm and 3.1 mm produced by merging BIMA and PdBI data show two different emission components: (i) the central cluster identified by Neri et al. (2007) and

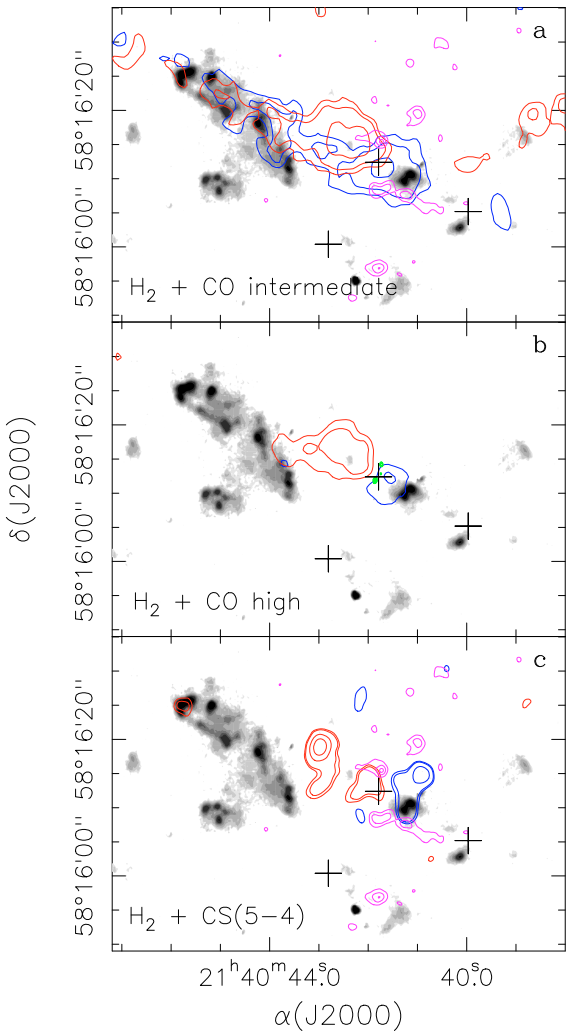

Fig. 7. Continuum 1.2 mm sources IRAM 2A and 41.73+12.8 (green contours in *the middle panel*) and contours of the integrated intensity of the N_2H^+ $J = 1 \rightarrow 0$ $F = 2 \rightarrow 1$ line (pink contours in *the upper and bottom panels*) superposed on the interferometric maps of the CO outflow published by Beltrán et al. (2001). Contours of the 1.2 mm continuum emission are 2.5, 3.0 to 21.0 by 3.0 mJy/beam. For the N_2H^+ integrated intensity emission, the contours are 27.3, 54.6, 81.9 mJy/beam × km s^{-1}. The grey scale is the 2.12 μm H_2 emission from Beltrán et al. (2009). Crosses indicate the positions of BIMA 1, BIMA 2, and BIMA 3.

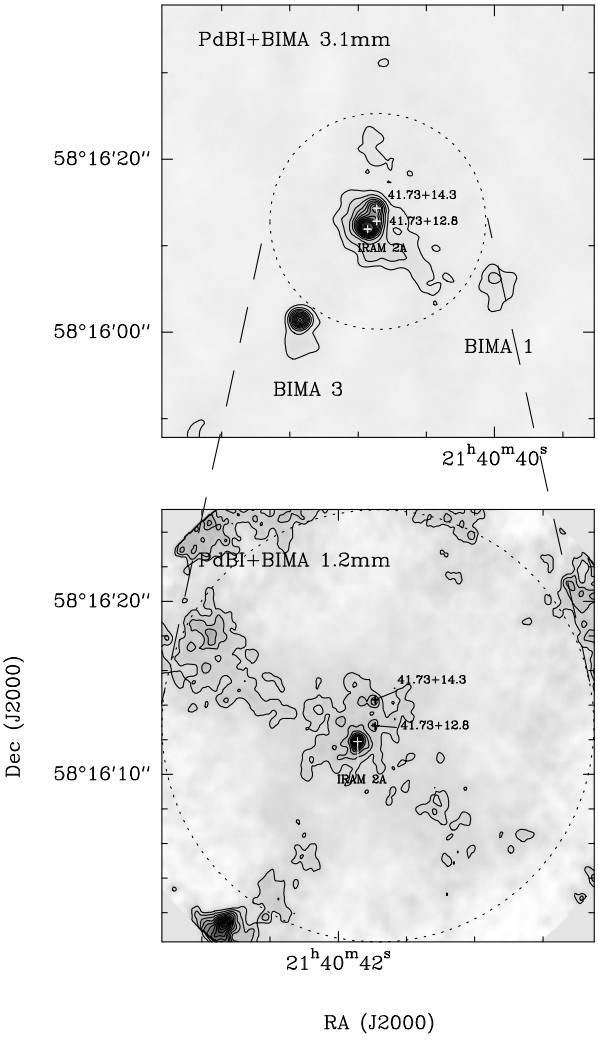

Fig. 8. PdBI+BIMA continuum images at 3.1 mm (*upper panel*) and 1.2 mm (*bottom panel*). Contours are: from 0.5 mJy/beam to 6 mJy/beam in steps of 0.5 mJy/beam in the 3.1 mm image, and from 3.5 mJy/beam to 39.5 mJy/beam in steps of 3.0 mJy/beam in the 1.2 mm continuum image. The primary beam of the PdBI at 1.2 mm is drawn in the panels.

(ii) extended emission along the outflow direction (see Fig. 8). The emission from the central cluster was modeled by Neri et al. (2007) who found that it could be explained as originating in three compact clumps (<300 AU) immersed in a cocoon of about ~2800 AU. The spectral indices are different for the cocoon and the compact cores. While the compact cores have spectral indices of ~1.4−1.9, the spectral index in the cocoon is ~2.8. The value in the cocoon is consistent with optically thin dust emission with $\beta \sim 1$.

The continuum emission at 1.2 mm and 3.1 mm extends along the outflow axis. This extended emission originates in the walls of the cavity excavated by the outflow, which are expected to be warmer than the surroundings. The dust continuum emission tracing the walls excavated by the outflow has also been observed in low-mass star-forming regions, as for example in the class 0 L1157 (Beltrán et al. 2004a). The spatial distribution of the continuum emission at 1.2 mm differs from that at 3.1 mm. The 1.2 mm emission is more intense in the eastern lobe. In contrast, the 3.1 mm emission comes mainly from the western lobe. This different spatial distribution could be indicative of a gradient in the 1.2 mm/3.1 mm spectral index along the outflow. While values higher than 2, consistent with optically thin dust emission, are found in the eastern (red) lobe, values ~0.6, typical of an ionized wind, are found in the western (blue) lobe. However, taking into account the technical complexity and the uncertainties involved in the merging processes of the PdBI and BIMA data, we must be cautious with this result. In regions with complex morphologies, the different filtering of the continuum emission at 3.1 mm and 1.2 mm (different synthesized beams) can produce an apparent change in the 1.2 mm/3.1 mm spectral index. A more complete set of data with visibilities that provide UV-coverage with critical sampling and consistent frequency scaling is required to confidently measure the 1.2 mm/3.1 mm spectral index.

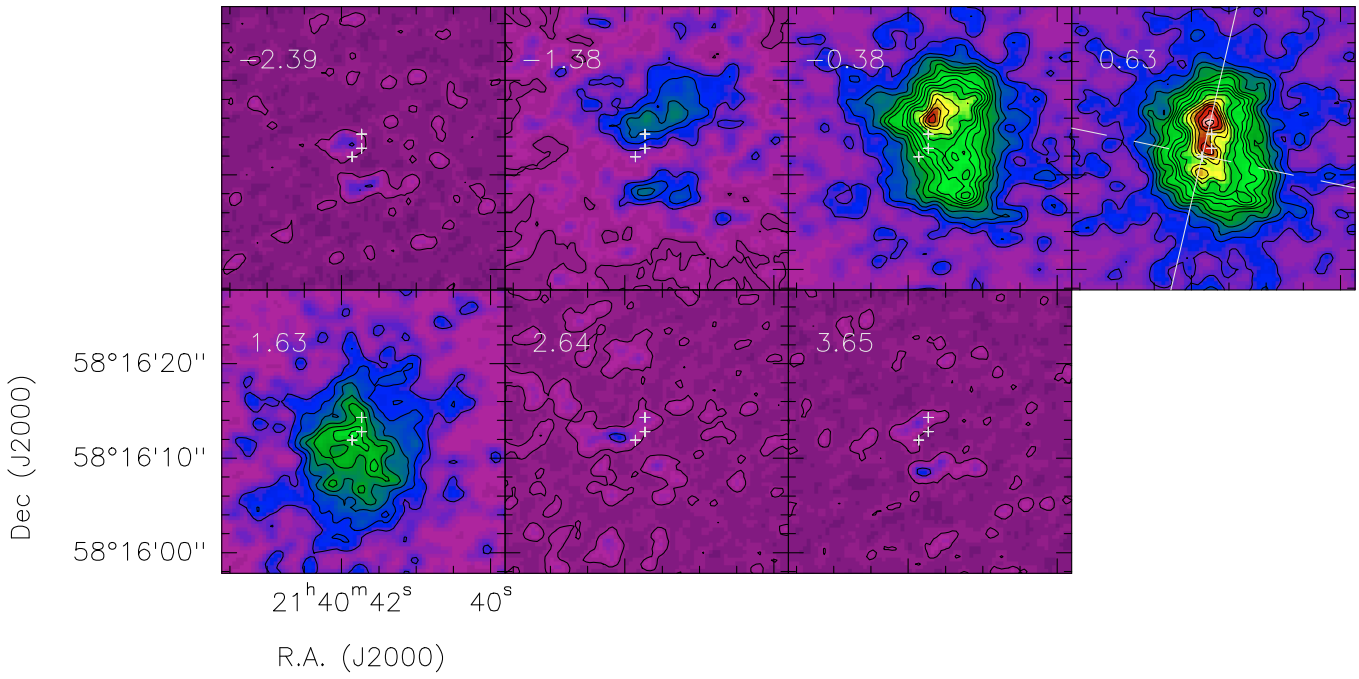

Fig. 9. Spectral intensity maps of the N_2H^+ $J = 1 \rightarrow 0$ $F = 2 \rightarrow 1$ line produced by combining the PdBI and 30 m data. Each panel is marked with the central velocity. Channel width is ∼1.0 km s^{-1}. Contours are from 5 mJy/beam to 380 mJy/beam in steps of 20 mJy/beam. In the panel labeled "0.63", we indicate the outflow direction (long dashed line) and the direction of the "waist" of gas and dust (solid line).

4.2. 30 m+PdBI N_2H^+ 1 → 0 image

We included the 30 m short spacing data and synthesized the 30 m+PdBI image to obtain a more realistic view of the spatial distribution of the N_2H^+ emission. After merging the 30 m and PdBI data, we obtained the image shown in Fig. 9. The highest red and blue shifted velocities show the same spatial distribution as the clumps N in the PdBI image (see the panels at 3.65 km s^{-1} and −1.38 km s^{-1} in Fig. 9). This high velocity gas is distributed in two filaments in the north and south of IRAM 2A, respectively. The bulk of the N_2H^+ emission, however, originates in an elongated envelope located perpendicular to the molecular outflow (see Figs. 7 and 8). This envelope exhibits a velocity gradient of ∼1 km s^{-1} over an angular distance of 11″ (∼23 km s^{-1} pc^{-1}) in the direction of the bipolar outflow. This velocity gradient is consistent with the outflow kinematics corroborating that the kinematics of the entire molecular globule is affected by the bipolar outflow.

The N_2H^+ envelope is elongated in the same orientation as the cocoon in the continuum model proposed by Neri et al. (2007). This suggests that both types of emission trace the same physical structure and that the different spatial distribution of the emission is caused by chemical differentiation. As discussed in Sect. 5, the [CH_3CN]/[N_2H^+] ratio is strongly dependent on the gas and dust temperature.

5. The CH_3CN/N_2H^+ abundance ratio: a chemical diagnostic

The different morphologies of CH_3CN and N_2H^+ can be at least qualitatively understood by considering that CH_3CN is mainly formed on the surface of dust grains (e.g., Bisschop et al. 2007; Garrod et al. 2008), whereas only gas phase processes are responsible for the formation and destruction of N_2H^+ (Aikawa et al. 2005). On the one hand, the N_2H^+ abundance increases in cold and dense regions, where CO molecules freeze-out onto dust grains. On the other hand, the largest fractional abundance of CH_3CN is observed toward warm regions (in particular hot cores), where the dust temperature becomes large enough (∼90 K) to allow mantle evaporation.

To illustrate how the dust temperature affects the CH_3CN/N_2H^+ abundance ratio, we consider a simple chemical model of a uniform cloud at temperatures of between 5 and 100 K. The chemical processes are the same as those described in detail by Caselli et al. (2008): gas phase formation and destruction of N_2H^+, HCO^+, H_3^+, and deuterated counterparts, time-dependent freeze-out of CO and N_2, thermal and non-thermal desorption due to cosmic-ray impulsive heating, and dust grains with a MRN (Mathis et al. 1977) size distribution. More details about the model can also be found in Emprechtinger et al. (2009).

For the CH_3CN chemistry, we used the results of the comprehensive Garrod et al. (2008) model M, shown in their Fig. 5. Here, the CH_3CN abundance is plotted as a function of time and temperature and exhibits two main plateau: one at $40 < T < 90$ K, where $X(CH_3CN) \sim 10^{-10}$, mainly due to HCN evaporation followed by gas phase processes, and one at $T > 90$ K, where $X(CH_3CN)$ reaches its peak abundance of 10^{-8} because of direct evaporation from grain mantles. At lower temperatures, $X(CH_3CN) < 10^{-13}$. To simulate this trend, our model assumes that a fraction ($X(CH_3CN) = 10^{-10}$) of CH_3CN on the surface of dust grains has a binding energy of 1900 K (close to that of CO), whereas the majority has a binding energy of 4500 K (close to that of H_2O).

Figure 10 shows the fractional abundances of CO, N_2H^+, and CH_3CN as a function of gas and dust temperature for three different values of the gas density: $n(H_2) = 5 \times 10^4$, 5×10^5 and 5×10^6 cm^{-3}. The gas and dust temperatures are assumed to be the same, given that they are coupled at densities higher than a few 10^4 cm^{-3} (Goldsmith 2001). We assume that the fraction

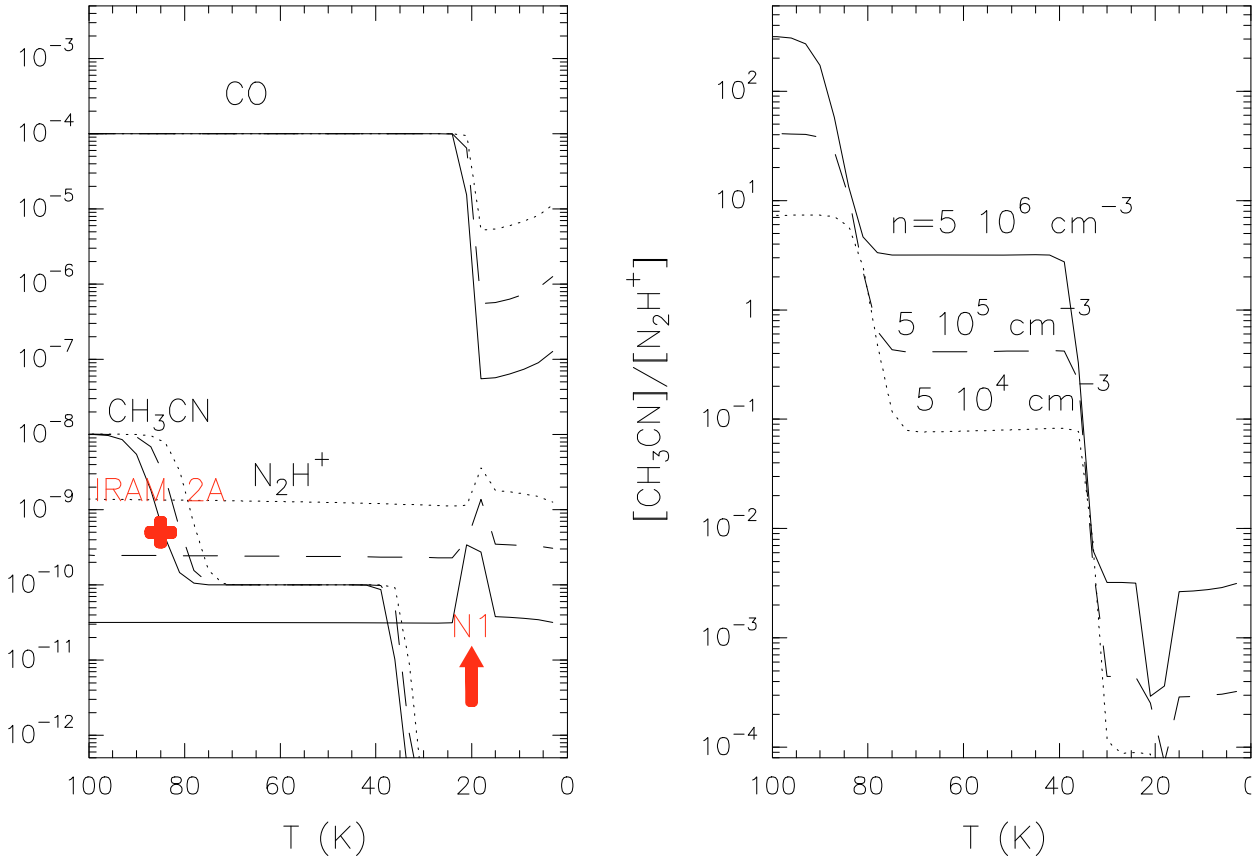

Fig. 10. Fractional abundances of CH_3CN, N_2H^+ and CO (*left*) and CH_3CN/N_2H^+ abundance ratio (*right*) as a function of the gas temperature for three different values of the molecular hydrogen density, 5×10^4 cm^{-3} (short dashed lines), 5×10^5 cm^{-3} (long dashed lines) and 5×10^6 cm^{-3} (solid lines).

of CH_3CN on the surface of dust grains does not change with density. Surface CO completely evaporates at $T > 20$ K. As expected, the N_2H^+ abundance shows a peak at the minimum of the CO abundance (CO is one of the main destroyers of N_2H^+, together with electrons and negatively charged dust grains). Being a molecular ion, N_2H^+ is sensitive to the volume density, given that the electron fraction varies approximately as $n(H_2)^{-0.5}$. The $[CH_3CN]/[N_2H^+]$ ratio as a function of temperature (and for the three different density values considered) is also plotted in Fig. 10. The model assumes a steady state.

The $[CH_3CN]/[N_2H^+]$ ratio varies by 5 orders of magnitude when the temperature increases from 20 to >100 K. This large variation makes this ratio an excellent chemical thermometer in this range of gas kinetic temperatures. Variation in the molecular hydrogen density can also affect this ratio but to a lesser extent. Since the N_2H^+ fractional abundance depends on the molecular hydrogen density, the $[CH_3CN]/[N_2H^+]$ ratio together with $X(N_2H^+)$ are excellent tracers of the temperature and the density of the emitting gas.

5.1. Molecular cores in IC 1396 N

On basis of our model results, we use chemistry as a diagnostic of the physical conditions in the cores of IC 1396 N. Towards IRAM 2A, we estimated that $X(CH_3CN) \sim 5 \times 10^{-10}$ and $X(N_2H^+) < 1.2 \times 10^{-10}$. The $[CH_3CN]/[N_2H^+]$ ratio and the derived $X(CH_3CN)$ are consistent with our chemical model for gas temperatures ~80 K, in agreement with our estimate of the gas temperature from the CH_3CN rotational diagram. The upper limit to the N_2H^+ abundance derived towards this core suggests that the molecular hydrogen density is $>5 \times 10^5$ cm^{-3}, which is also consistent with the masses and sizes derived from the continuum emission. The CH_3CN abundance measured towards IRAM 2A is similar to that found in hot corinos (Bottinelli et al. 2004, 2007) but 1 to 2 orders of magnitude lower than those expected in high-mass cores (Nummelin et al. 2000; Wilner et al. 1994). Fuente et al. (2005b) derived a CH_3CN abundance of $\sim 7 \times 10^{-9}$ towards the IM core NGC 7129−FIRS 2, which is more similar to the values found in high mass stars. NGC 7129−FIRS 2 and IC 1396 N are IM protostars with similar luminosities. The difference in the CH_3CN abundance of NGC 7129−FIRS 2 and IC 1396 N may be caused by IC 1396 N being a cluster of low-mass and Herbig Ae stars. In contrast, Fuente et al. (2005b) did not detect clustering in NGC 7129−FIRS 2 down to a scale of ~1000 AU, which suggests that NGC 7129–FIRS 2 could be the precursor of a more massive Be star. On the other hand, IC 1396 N is a more evolved object than NGC 7129–FIRS 2. While IC 1396 N is considered a borderline class 0/I object, NGC 7129–FIRS 2 is one of the youngest class 0 objects ever observed (Fuente et al. 2001, 2005a). The other possibility is that the low abundance of CH_3CN is caused by a small (undetectable with our angular resolution) photodissociation region (PDR) already formed by the nascent IM star. A PDR of $A_v \sim 1-3$ mag, at a density of $n(H_2) = 5 \times 10^5$ cm^{-3}, would have a size of a few 100 AU. The CH_3CN $5_k \rightarrow 4_k$ and N_2H^+ $1 \rightarrow 0$ lines have not been detected

Table 1. Molecular cores in IC 1396 N.

Source	RA(2000)	Dec(2000)	Size	T (K)	Mass ($M_\odot$)	$N(H_2)$ (cm^{-2})	$X(N_2H^+)$	$X(CH_3CN)$	$[CH_3CN]/[N_2H^+]$	Δv ($km\,s^{-1}$)
IRAM 2A*	21:40:41.86	58:16:11.9	$0.4'' \times 0.2''$	**100**	**0.06**	$\mathbf{3.1 \times 10^{24}}$	$\mathbf{<1.4 \times 10^{-10}}$	$\mathbf{\sim 5.0 \times 10^{-10}}$	>4	~2
BIMA3*	21:40:42.84	58:16:01.4	$0.8'' \times 0.4''$	**100**	**0.05**	$\mathbf{6.5 \times 10^{23}}$	$\mathbf{<1.6 \times 10^{-10}}$	$\mathbf{<2.3 \times 10^{-9}}$		~2
				50	0.11	1.4×10^{24}	$<4.1 \times 10^{-11}$	$<1.2 \times 10^{-9}$		
				20	0.32	4.1×10^{24}	$<6.2 \times 10^{-12}$	$<6.1 \times 10^{-10}$		
N1[a]	21:40:41.76	58:16:15.57	$1.4'' \times 1.2''$	100	<0.03	$<6.8 \times 10^{22}$	$>1.8 \times 10^{-9}$		<2	2.4
				50	<0.06	$<1.4 \times 10^{23}$	$>4.7 \times 10^{-10}$		<5	
				20	**<0.15**	$\mathbf{<3.7 \times 10^{23}}$	$\mathbf{>8.0 \times 10^{-11}}$		<16	
N2[a]	21:40:41.03	58:16:18.66	$1.4'' \times 1.2''$	100	<0.03	$<6.8 \times 10^{22}$	$>1.1 \times 10^{-9}$		<5	2.1
				50	<0.06	$<1.4 \times 10^{23}$	$>3.0 \times 10^{-10}$		<8	
				20	**<0.15**	$\mathbf{<3.7 \times 10^{23}}$	$\mathbf{>5.1 \times 10^{-11}}$		<40	
N3[a]	21:40:41.83	58:16:08.22	$1.4'' \times 1.2''$	100	<0.03	$<6.8 \times 10^{22}$	$>1.6 \times 10^{-9}$		<2	1.9
				50	<0.06	$<1.4 \times 10^{23}$	$>4.2 \times 10^{-10}$		<5	
				20	**<0.15**	$\mathbf{<3.7 \times 10^{23}}$	$\mathbf{>7.2 \times 10^{-11}}$		<17	
N4[a]	21:40:41.22	58:16:07.26	$1.4'' \times 1.2''$	100	<0.03	$<6.8 \times 10^{22}$	$>1.2 \times 10^{-9}$		<3	2.4
				50	<0.06	$<1.4 \times 10^{23}$	$>3.1 \times 10^{-10}$		<7	
				20	**<0.15**	$\mathbf{<3.7 \times 10^{23}}$	$\mathbf{>5.3 \times 10^{-11}}$		<36	
N5[a]	21:40:41.81	58:15:56.82	$1.4'' \times 1.2''$	100	<0.03	$<6.8 \times 10^{22}$	$>1.3 \times 10^{-9}$		<3	2.1
				50	<0.06	$<1.4 \times 10^{23}$	$>3.4 \times 10^{-10}$		<7	
				20	**<0.15**	$\mathbf{<3.7 \times 10^{23}}$	$\mathbf{>5.8 \times 10^{-11}}$		<20	

* Sizes, masses and $N(H_2)$ from Neri et al. (2007); [a] the size is assumed to be equal to the beam size. The values of $N(H_2)$ and the masses have been estimated from the 3 × rms (1 mJy/beam) of our 3.1 mm map and by adopting $\kappa_{1\ mm} = 0.01\ cm^2\ g^{-1}$ and a dust emissivity spectral index of 1.

towards BIMA 3. The non-detection of this core in N_2H^+ is consistent with its very high density ($n(H_2) > 5 \times 10^5\ cm^{-3}$) and hot (~100 K) gas.

In addition to the IRAM 2A and BIMA 3 cores, we have detected filaments and clumps in the N_2H^+ $1 \rightarrow 0$ line emission that remain undetected in the other tracers. In Table 2, we show the derived N_2H^+ column densities towards 5 selected positions (labeled N in Fig. 4 and Table 2) assuming gas temperatures of 100, 50, and 20 K. These column densities are lower limits to the true values since the emission close to the ambient velocities could be underestimated because of the PdBI filtering. We also show lower limits to the N_2H^+ abundance and upper limits to the $[CH_3CN]/[N_2H^+]$ ratio. Comparing the $[CH_3CN]/[N_2H^+]$ ratio with our chemical calculations (see Fig. 10), we estimate an upper limit of 50 K for the true gas temperature. However, assuming that $T \sim 50$ K, the derived N_2H^+ abundance would be 1 order of magnitude higher than predicted by our chemical model for reasonable values of the molecular hydrogen density ($\sim 5 \times 10^5\ cm^{-3}$). Thus, we conclude that probably these clumps have gas temperatures of around 20 K or less. We note that our chemical model predicts a peak in N_2H^+ abundance at temperatures of around $T = 17$ K. The UV radiation from the star and the possible low velocity shocks heat the walls of the cavity excavated by the bipolar outflow. In addition to the density and column density enhancements expected in the walls of the cavity, the detection of clumps N1 to N4 might be favored by the warmer gas.

Summarizing, we have detected two chemically different regions in IC 1396 N: (i) the warm cores IRAM 2A and BIMA 3, detected in continuum emission and with temperatures around 100 K and (ii) the filaments and the clumps N1 to N4 located along the walls of the bipolar cavity excavated by the outflow that are only detected in the N_2H^+ $1 \rightarrow 0$ line and probably have temperatures of around 20 K. N5 could be a colder and denser one. The $[CH_3CN]/[N_2H^+]$ ratio is a good chemical diagnostic for discerning the temperature of the dense cores.

6. Overview of the region

Figure 11 shows a sketch of the cometary bright-rimmed globule IC 1396 N. The bipolar molecular outflow associated with the young IM protostar has excavated the molecular cloud producing a biconical cavity. This cavity has disrupted the cloud in the south-western direction allowing the high-velocity gas to travel away. The dense gas is located in an elongated feature, probably an asymmetric toroid, in the direction perpendicular to the outflow. The molecular toroid presents strong temperature gradients, which produce a chemical differentiation.

The N_2H^+ emission is very intense in the outer part of the toroid, being the peaks located ~3″ north and south of the position of the protocluster (see Fig. 9), but is absent in the inner region. The inner region was modeled by Neri et al. (2007) based on continuum data. They concluded that the continuum emission originates in 3 dense cores immersed in a cocoon. The non detection of these cores in N_2H^+ suggest that all three are warm cores, probably protostars. Consequently, the previously understood to be a single IM protostar, could be a compact protocluster. Emission of the CH_3CN $5_k \rightarrow 4_k$ and $13_k \rightarrow 12_k$ lines has been detected towards the most intense core, IRAM 2A (Neri et al. 2007, this work). On the basis of our CH_3CN observations, we determine a temperature of 97 ± 25 K and a CH_3CN abundance of $5 \pm 3 \times 10^{-10}$ towards IRAM 2A, similar to that found in hot corinos.

Summarizing, the strong dependence of the $[CH_3CN]/[N_2H^+]$ on the gas and dust temperature produces a layered structure in the molecular toroid perpendicular to the bipolar outflow, the CH_3CN emission being more intense in the inner region and N_2H^+ in the outer parts.

6.1. Source(s) of the molecular outflow(s)

Three bipolar outflows have been identified in the CO maps: the first one is located around the position of the strong mm

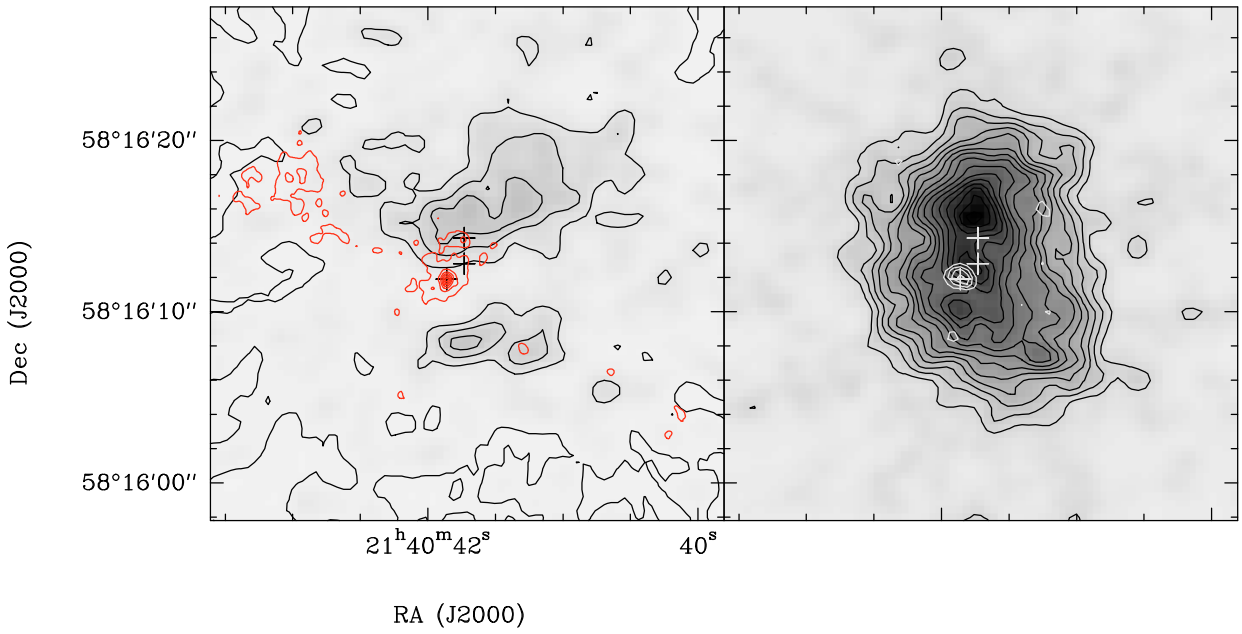

Fig. 11. *Left*: spectral map of the N_2H^+ 1 → 0 line emission produced by combining our PdBI and 30 m data at a velocity of −1.4 km s^{-1} (grey scale map). This blue-shifted emission delineates the walls of the cavity excavated by the outflow. We have superposed the contours from 5 mJy/beam to 35 mJy/beam in steps of 5 mJy/beam of the 1.2 mm continuum emission BIMA+PdBI image (dashed red lines). *Right*: spectral map of the N_2H^+ 1 → 0 line emission produced by combining our PdBI and 30 m data at the ambient velocity, ~0.63 km s^{-1} (grey scale map). In solid white contours, we show the integrated intensity PdBI map of the CH_3CN $5_k \rightarrow 4_k$ line.

continuum source BIMA 2, in the head of the globule, the second one is associated with BIMA 1 (Beltrán et al. 2002), and the last one is located in the northern region, outside our interferometric images (Codella et al. 2001). Single-dish observations of the SiO lines towards the central outflow (that associated with BIMA 2) detected a highly collimated structure with four clumps of sizes <0.1 pc located along the outflow axis. Interferometric images of the CO emission, however, showed that this outflow exhibits a complex morphology that Beltrán et al. (2002) interpreted as being the result of the interaction of the high velocity gas with dense clumps surrounding the protostar.

Our highest angular resolution images have allowed us to learn more about the structure of this complex bipolar outflow. One of the main questions is the driving source of this energetic outflow. The mm source BIMA 2, previously understood to be a unique IM protostar, was found to be a cluster of dense cores. The detection of warm CH_3CN in IRAM 2A implies that this is the most massive protostar and could be the driving source of this energetic outflow. This interpretation is also supported by the morphology of the 1 mm continuum emission. However the angular resolution of previous interferometric CO observations (~2″) did not allow us to decide this conclusion with confidence (see Fig. 7). Higher angular resolution observations of CO and/or SiO are required to determine the outflow(s) exciting source(s).

7. Conclusions

We have carried out high-angular resolution (1.4″) observations of the continuum at 3.1 mm and of the N_2H^+ 1 → 0 and CH_3CN $5_k \rightarrow 4_k$ lines using the Plateau de Bure Interferometer (PdBI). In addition, we have merged the PdBI images with previous BIMA (continuum data at 1.2 mm and 3.1 mm) and single-dish (N_2H^+) data to obtain a comprehensive description of the region. Our results can be summarized as follows:

- On large scales, the combination of our data with previous BIMA and 30 m data show that the associated bipolar outflow has completely eroded the initial molecular globule. The 1.2 mm and 3.1 mm continuum emission is extended along the outflow axis tracing the warm walls of the biconical cavity.
- Most of the molecular gas is located in an elongated feature in the direction perpendicular to the outflow. Our results show two types of region in IC 1396 N: (i) the cores detected in dust continuum emission, one of which (the most massive) has also been detected in the CH_3CN $5_k \rightarrow 4_k$ line; and (ii) the filaments and clumps located in the molecular toroid, mainly along the walls of the bipolar cavity excavated by the outflow, which are only detected in the N_2H^+ 1 → 0 line. This chemical differentiation can be understood in terms of the temperature dependent behavior of the chemistry of N_2H^+ and CH_3CN. The [CH_3CN]/[N_2H^+] ratio increases by 5 orders of magnitude when the gas temperature increases from 20 to 100 K.
- We have used the [CH_3CN]/[N_2H^+] ratio as a chemical diagnostic to derive the temperature and evolutionary status of the young stellar objects (YSOs). The CH_3CN abundance towards IRAM 2A is similar to that found in hot corinos and lower than that expected towards IM and high mass hot cores. This could indicate that IRAM 2A is a low mass or a Herbig Ae star instead of the precursor of a massive Be star. Alternatively, the low CH_3CN abundance could be the consequence of IRAM 2A being a class 0/I transition object that has already formed a small photodissociation region (PDR).

Our chemical model and observational data prove that the [CH_3CN]/[N_2H^+] ratio is a good tracer of the gas kinetic

temperature that is closely related to the spectral type of the star that has been formed. Together with the $[CH_3CN]/[N_2H^+]$ ratio, the fractional abundances of CH_3CN and N_2H^+ provide us with information about the physical conditions of the gas. Interferometric observations of CH_3CN and N_2H^+ towards IM protostars are, consequently, a valuable tool for obtaining insight into the structure of these young stellar objects.

Acknowledgements. We are grateful to the IRAM staff in Grenoble and Spain with their great help during the observations and data reduction.

References

Alonso-Albi, T., Fuente, A., Bachiller, R., et al. 2008, ApJ, 680, 1289
Alonso-Albi, T., Fuente, A., Bachiller, R., et al. 2009, A&A, 497, 117
Aikawa, Y., Herbst, E., Roberts, H., & Caselli, P. 2005, ApJ, 620, 330
Beltrán, M. T., Girart, J. M., Estalella, R., Ho, P. T. P., & Palau, A. 2002, ApJ, 573, 246
Beltrán, M. T., Gueth, F., Guilloteau, S., & Dutrey, A. 2004a, A&A, 416, 631
Beltrán, M. T., Girart, J. M., Estalella, R., & Ho, P. T. P. 2004b, A&A, 426, 941
Beltrán, M. T., Massi, F., López, R., Girart, J. M., & Estalella, R. 2009, A&A, 504, 97
Bisschop, S. E., Jørgensen, J. K., van Dishoeck, E. F., & de Wachter, E. B. M. 2007, A&A, 465, 913
Bottinelli, S., Ceccarelli, C., Neri, R., et al. 2004, ApJ, 617, L69
Bottinelli, S., Ceccarelli, C., Williams, J. P., & Lefloch, B. 2007, A&A, 463, 601
Caselli, P., Vastel, C., Ceccarelli, C., et al. 2008, A&A, 492, 703
Codella, C., Bachiller, R., Nisini, B., Saraceno, P., & Testi, L. 2001, A&A, 376, 271
Emprechtinger, M., Caselli, P., Volgenau, N. H., Stutzki, J., & Wiedner, M. C. 2009, A&A, 493, 89
Fuente, A., Neri, R., Martín-Pintado, J., et al. 2001, A&A, 366, 873
Fuente, A., Rodríguez-Franco, A., Testi, L., et al. 2003, ApJ, 598, L39
Fuente, A., Neri, R., & Caselli, P. 2005a, A&A, 444, 481
Fuente, A., Rizzo, J. R., Caselli, P., Bachiller, R., & Henkel, C. 2005b, A&A, 433, 535
Fuente, A., Alonso-Albi, T., Bachiller, R., et al. 2006, ApJ, 649, L119
Garrod, R. T., Weaver, S. L. W., & Herbst, E. 2008, ApJ, 682, 283
Goldsmith, P. F. 2001, ApJ, 557, 736
Mathis, J. S., Rumpl, W., & Nordsieck, K. H. 1977, ApJ, 217, 425
Neri, R., Fuente, A., Ceccarelli, C., et al. 2007, A&A, 468, L33
Nisini, B., Massi, F., Vitali, F., et al. 2001, A&A, 376, 553
Nummelin, A., Bergman, P., Hjalmarson, Å., et al. 2000, ApJS, 128, 213
Wilner, D. J., Wright, M. C. H., & Plambeck, R. L. 1994, ApJ, 422, 642